

## Article

# Sensorless Control of Surfaced-Mounted Permanent Magnet Synchronous Motor in a Wide-Speed Range

Xiang Li, Yuze Cui and Xinzhang Wu \*

State Key Laboratory of Featured Metal Materials and Life-Cycle Safety for Composite Structures,  
Guangxi University, Nanning 530004, China; xiangli@gxu.edu.cn (X.L.); 2112301011@st.gxu.edu.cn (Y.C.)

\* Correspondence: xwu@gxu.edu.cn

**Abstract:** This paper delves into a comprehensive study of a wide-speed-range sensorless control approach for surface-mounted permanent magnet synchronous motors (SPMSMs). In the low-speed range, a novel high-frequency pulse voltage injection (HFPVI) method is introduced for rotor position estimation, which does not depend on motor saliency and is well-suited for SPMSMs. This method incorporates a second-order generalized integrator (SOGI) and a new modulation signal to enhance the accuracy of rotor position estimation. For medium-to-high speeds, an improved super-twisting sliding mode observer (STSMO) utilizing a continuous hyperbolic tangent function is proposed to mitigate chattering. Additionally, a new phase-locked loop (NPLL) is introduced to accurately obtain the rotor position. Furthermore, this paper designs an exponential weighted switching function to facilitate a smooth transition of the motor from the low-speed domain to the medium- and high-speed domains. The effectiveness and superiority of the proposed methods are validated through simulations and experiments conducted on an RTU-BOX platform. The rotor position estimation errors of the proposed new HFPVI method and the improved STSMO method under various operating conditions are both approximately 0.05 rad (2.8 elc-deg), and the SPMSM can switch smoothly from the low-speed range to the medium- and high-speed ranges.

**Keywords:** surface-mounted permanent magnet synchronous motor (SPMSM); wide-speed range sensorless control; high-frequency pulse voltage injection (HFPVI) method; super-twisting sliding mode observer (STSMO)



**Citation:** Li, X.; Cui, Y.; Wu, X.  
Sensorless Control of Surfaced-Mounted Permanent Magnet Synchronous Motor in a Wide-Speed Range. *Electronics* **2024**, *13*, 1131.  
<https://doi.org/10.3390/electronics13061131>

Academic Editors: Claudio Rossi and Yasser Gritli

Received: 29 January 2024

Revised: 8 March 2024

Accepted: 17 March 2024

Published: 20 March 2024



**Copyright:** © 2024 by the authors. Licensee MDPI, Basel, Switzerland. This article is an open access article distributed under the terms and conditions of the Creative Commons Attribution (CC BY) license (<https://creativecommons.org/licenses/by/4.0/>).

## 1. Introduction

Permanent magnet synchronous motors (PMSMs) are widely utilized in industrial manufacturing, household appliances, and various other fields due to their compact size, robust structure, high power density, and excellent speed regulation capabilities. The use of mechanical sensors in PMSMs poses challenges such as large size, high cost, and complex wiring. As a result, sensorless control has emerged as a significant research focus in the control field of PMSM. Sensorless control methods for PMSMs can be categorized into two main types based on the speed ranges at which the motor operates: high-frequency injection (HFI) methods and model-based methods [1–4]. HFI methods are primarily suitable for low speeds, where high-frequency signals are injected into the motor to obtain the rotor angle position based on motor saliency [5,6]. On the other hand, model-based methods rely on the back electromotive force (EMF) of the motor to estimate the rotor angle position. These methods are not effective at low speeds because the motor back EMF is minimal, making it challenging to accurately obtain the rotor angle position. In contrast, at medium-to-high speeds, the motor back EMF provides sufficient information for precise rotor angle estimation, making model-based methods more suitable. In situations that involve operations across both low and medium-to-high speeds, integrating both high-frequency injection and model-based methods is essential for achieving sensorless control over a wide-speed range. By combining these two control strategies tailored for

different speed domains, comprehensive sensorless control for PMSMs in a wide-speed range can be realized.

HFI methods can be categorized into different types, including high-frequency rotating voltage injection (HFRVI) method [7–9], high-frequency pulsating voltage injection (HFPVI) method [10–12], and high-frequency square wave voltage injection (HFSVI) method [13–15]. The HFRVI method involves injecting high-frequency sinusoidal voltage into the three-phase stator of the motor, which is not suitable for SPMSMs. On the other hand, the HFPVI method injects sinusoidal high-frequency voltage into the estimated d-axis of the motor to saturate the magnetic circuit, create a difference in the d–q axis inductances, and then determine the rotor position based on the saturated saliency of the motor. This method features a straightforward demodulation process and is well-suited for SPMSMs. In comparison, the HFSVI method is similar to the HFPVI method but involves injecting a high-frequency square wave voltage instead. In [16], a second-order generalized integrator (SOGI) is employed instead of the traditional bandpass filter (BPF) to reduce phase delay. However, all these methods are dependent on motor saliency. For SPMSMs, a substantial voltage amplitude is required to induce saturated saliency in the motor, resulting in increased noise levels.

The model-based methods mainly include the flux linkage observation method [17–19], model reference adaptive system method [20–22], sliding mode observer (SMO) method [23–25], and extended Kalman filter method [26–28]. The flux observation method obtains the angle position of the rotor by directly calculating the motor's flux linkage with sampling voltage and current, which relies on the precision of the motor model. The model reference adaptive system method obtains the rotor's angle position on the basis of the mathematical model of the motor, so the accuracy of motor parameters will affect the observation accuracy. The extended Kalman filter method has strong anti-interference ability, but the calculation is very complicated. The SMO method has advantages such as simple structure, strong robustness, parameter changes that have little impact on the observation accuracy, etc., and is extensively employed in sensorless control of PMSMs. However, the switching property of the SMO will result in chattering due to the system moving back and forth on the sliding mode surface, which deteriorates the estimation precision. In [29], the sign function is adopted, which leads to significant chattering, and then a low pass filter (LPF) is necessary to improve the estimation accuracy. In [30,31], to eliminate the chattering and avoid using the LPF, the continuous sigmoid function and hyperbolic function are employed as alternatives to the sign function. In [32,33], a super-twisting sliding mode observer (STSMO) is utilized, and its effectiveness in suppressing chattering is validated through simulations and experiments. For the SMO, a phase-locked loop (PLL) is widely employed to estimate the rotor's position and speed. In [34], a traditional PLL is introduced for the estimation of the rotor's speed and position of PMSM. However, a certain estimation error exists, prompting the exploration of alternative methods to improve accuracy.

To achieve a smooth transition of the motor from low speed to medium and high speeds, a suitable switching strategy is essential, as the sensorless control techniques differ between these speed ranges. The most frequently adopted switching methods include the hysteresis switching and the weighted switching method [17,35]. The hysteresis switching method is relatively simple but may cause position and speed fluctuations [35]. The weighted switching method generally weights the rotational speed or position. Compared with the hysteresis switching method, the weighted switching approach is more effective in reducing fluctuations in both position and speed within the transition zone.

The main contributions of the paper are as follows: (1) proposing a new HFPVI method that does not rely on motor saliency and is suitable for the SPMSM. In addition, a SOGI and a new modulation signal are adopted to enhance the estimation position accuracy of the rotor. (2) Proposing an improved STSMO that uses a continuous hyperbolic tangent function to reduce chattering and introduces an NPLL to accurately estimate the rotor position. (3) Designing an exponential weighted switching function to facilitate a seamless

transition between the two control methods in the transition interval. (4) Validating the effectiveness of the above method through simulation and experiments on a 1.5 kW SPMSM.

## 2. Sensorless Control Methods for SPMSM

### 2.1. New HFPVI Method

This section proposes a new HFPVI method that is essentially different in principle from the traditional HFPVI method. It injects high-frequency voltage into the estimated  $d$ -axis of the motor, and the current is extracted from the  $\alpha - \beta$  axis. Then, a SOGI is employed to replace the traditional BPF for extracting high-frequency components, and a new modulation signal is designed for frequency separation, which enhances the rotor position estimation accuracy.

Under high-frequency excitation, the voltage equation of PMSM can be written as follows:

$$\begin{bmatrix} u_d \\ u_q \end{bmatrix} = R_s \begin{bmatrix} i_d \\ i_q \end{bmatrix} + \begin{bmatrix} L_d & 0 \\ 0 & L_q \end{bmatrix} \frac{d}{dt} \begin{bmatrix} i_d \\ i_q \end{bmatrix} + \omega_e \begin{bmatrix} -L_q i_q \\ L_d i_d + \psi_f \end{bmatrix} \quad (1)$$

where  $u_d$  and  $u_q$  are the  $d - q$  axis voltages, respectively,  $i_d$  and  $i_q$  are the  $d - q$  axis currents, respectively,  $L_d$  and  $L_q$  are the  $d - q$  axis inductances of the motor, respectively,  $\omega_e$  is the motor electrical angular velocity, and  $\psi_f$  is the motor flux linkage.

When the motor runs at a low speed, the motor's electrical speed  $\omega_e$  is small, the fundamental frequency of the motor is negligible compared to the frequency of the injected high-frequency pulse voltage, and resistance is negligible compared to high-frequency inductance. Therefore, Equation (1) can be simplified as follows:

$$\begin{bmatrix} u_{dh} \\ u_{qh} \end{bmatrix} = \begin{bmatrix} L_d & 0 \\ 0 & L_q \end{bmatrix} \frac{d}{dt} \begin{bmatrix} i_{dh} \\ i_{qh} \end{bmatrix} \quad (2)$$

where  $u_{dh}$  and  $u_{qh}$  are the high-frequency voltages in the  $d - q$  axis, respectively, and  $i_{dh}$  and  $i_{qh}$  are the high-frequency currents, respectively.

Figure 1 depicts the transformation relationship between the stationary  $\alpha - \beta$  axis, the actual  $d - q$  axis, and the estimated  $\hat{d} - \hat{q}$  axis.  $\Delta\theta$  is the angle position error of the rotor, that is,  $\Delta\theta = \theta - \hat{\theta}$ , where  $\theta$  is the actual position of the rotor,  $\hat{\theta}$  is the estimated position of the rotor.

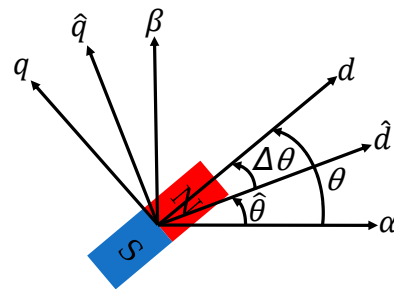


**Figure 1.** Transformation relationship between the stationary  $\alpha - \beta$  axis, the actual  $d - q$  axis, and the estimated  $\hat{d} - \hat{q}$  axis.

According to the relationship between each axis system shown in Figure 1 and the mathematical model Equation (2), the high-frequency voltage can be obtained as follows:

$$\begin{bmatrix} u_{dh} \\ u_{qh} \end{bmatrix} = \begin{bmatrix} L_d & 0 \\ 0 & L_q \end{bmatrix} \frac{d}{dt} \begin{bmatrix} i_{dh} \\ i_{qh} \end{bmatrix} = \begin{bmatrix} L_d & 0 \\ 0 & L_q \end{bmatrix} \begin{bmatrix} \cos\theta & \sin\theta \\ -\sin\theta & \cos\theta \end{bmatrix} \frac{d}{dt} \begin{bmatrix} i_{\alpha h} \\ i_{\beta h} \end{bmatrix} \quad (3)$$

where  $i_{\alpha h}$  and  $i_{\beta h}$  are the high-frequency currents in the  $\alpha - \beta$  axis, respectively.

On the basis of the principle of coordinate transformation, the relationship of high-frequency voltage in the  $d - q$  axis and the  $\hat{d} - \hat{q}$  axis can be obtained as follows:

$$\begin{bmatrix} u_{dh} \\ u_{qh} \end{bmatrix} = \begin{bmatrix} \cos(\Delta\theta) & \sin(\Delta\theta) \\ -\sin(\Delta\theta) & \cos(\Delta\theta) \end{bmatrix} \begin{bmatrix} \hat{u}_{dh} \\ \hat{u}_{qh} \end{bmatrix} \quad (4)$$

Assuming that the voltage injected into the estimated  $\hat{d} - \hat{q}$  axis is as bellow:

$$\begin{bmatrix} \hat{u}_{dh} \\ \hat{u}_{qh} \end{bmatrix} = \begin{bmatrix} U_h \cos(\omega_h t) \\ 0 \end{bmatrix} \quad (5)$$

where  $\hat{u}_{dh}$  and  $\hat{u}_{qh}$  are the high-frequency voltages injected into the  $\hat{d} - \hat{q}$  axis, respectively, and  $U_h$  and  $\omega_h$  are the amplitude and angular frequency of the injected high-frequency voltage, respectively.

Substituting Equations (4) and (5) into Equation (3):

$$\begin{aligned} \frac{d}{dt} \begin{bmatrix} i_{\alpha h} \\ i_{\beta h} \end{bmatrix} &= \begin{bmatrix} \cos \theta & -\sin \theta \\ \sin \theta & \cos \theta \end{bmatrix} \begin{bmatrix} \frac{1}{L_d} & 0 \\ 0 & \frac{1}{L_q} \end{bmatrix} \begin{bmatrix} \cos(\Delta\theta) & -\sin(\Delta\theta) \\ \sin(\Delta\theta) & \cos(\Delta\theta) \end{bmatrix} \begin{bmatrix} \hat{u}_{dh} \\ \hat{u}_{qh} \end{bmatrix} \\ &= \begin{bmatrix} \cos \theta & -\sin \theta \\ \sin \theta & \cos \theta \end{bmatrix} \begin{bmatrix} \frac{1}{L_d} & 0 \\ 0 & \frac{1}{L_q} \end{bmatrix} \begin{bmatrix} \cos(\Delta\theta) & -\sin(\Delta\theta) \\ \sin(\Delta\theta) & \cos(\Delta\theta) \end{bmatrix} \begin{bmatrix} U_h \cos(\omega_h t) \\ 0 \end{bmatrix} \end{aligned} \quad (6)$$

From Equation (6), the current with high frequency in the  $\alpha - \beta$  axis can be expressed as follows:

$$\begin{bmatrix} i_{\alpha h} \\ i_{\beta h} \end{bmatrix} = \frac{U_h}{\omega_h} \begin{bmatrix} \frac{\cos\theta\cos(\Delta\theta)}{L_d} + \frac{\sin\theta\sin(\Delta\theta)}{L_q} \\ \frac{\sin\theta\cos(\Delta\theta)}{L_d} - \frac{\cos\theta\sin(\Delta\theta)}{L_q} \end{bmatrix} \sin(\omega_h t) \quad (7)$$

The above formula is the response current of the stationary  $\alpha - \beta$  axis coordinate system under high-frequency excitation. When the rotor's estimated angle position converges to the actual value,  $\Delta\theta$  is small enough, which can be written as follows:

$$\begin{bmatrix} i_{\alpha h} \\ i_{\beta h} \end{bmatrix} = \frac{U_h}{\omega_h L_d} \begin{bmatrix} \cos \theta \\ \sin \theta \end{bmatrix} \sin(\omega_h t) \quad (8)$$

It can be seen that  $i_{\alpha h}$  and  $i_{\beta h}$  contain rotor position information. The traditional HFPVI method uses BPF to extract high-frequency current signals, but it will cause phase lag and reduce the angle position estimation accuracy of the rotor. To avoid using BPF, a SOGI is used instead of BPF in this paper, which can reduce the amplitude attenuation and phase offset caused by BPF. The structure diagram of SOGI is illustrated in Figure 2. The parameter  $\omega_0$  is the frequency to be extracted, and output  $Y$  is the component of input  $X$  that only contains frequency  $\omega_0$ . The coefficient  $k$  affects the filtering effect of SOGI; the smaller the  $k$  chosen, the better the filtering effect is, but the slower the response speed of the filter is. Therefore,  $k$  needs to be determined after weighing the filtering effect and response speed. The transfer function of SOGI is as follows:

$$G(s) = \frac{k\omega_0 s}{s^2 + k\omega_0 s + \omega_0^2} \quad (9)$$

The parameter  $k$  affects the filtering characteristics of SOGI. Therefore, parameter  $k$  needs to be determined after weighing the filtering effect and response speed, combining the filtering effect in actual experiments. Figure 3 depicts the amplitude–frequency and phase–frequency curves corresponding to different  $k$  values of SOGI. The filtering effect of SOGI becomes better and better as the  $k$  value decreases. The value of  $k$  is chosen as 0.1 in this paper, except for the center frequency; the other frequencies are well attenuated.



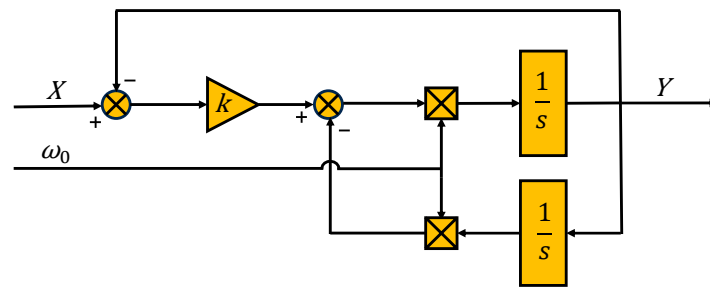


**Figure 2.** The structure diagram of SOGI.

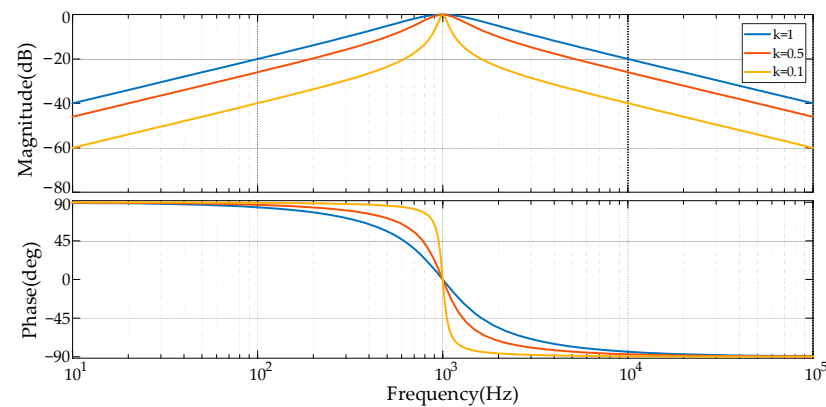


**Figure 3.** Phase–frequency and amplitude–frequency characteristic curves comparison of SOGI.

After being extracted by SOGI, the high-frequency current signals containing the rotor position need to be multiplied by the modulation signal. A new modulation function  $\cos(\omega_h t)\sin(2\omega_h t)$  is introduced in this paper, which is multiplied by the corresponding high-frequency current in the  $\alpha - \beta$  axis and then passed through *LPF*, the modulated current can be expressed as follows:

$$\begin{aligned}
 \begin{bmatrix} i_{\alpha l} \\ i_{\beta l} \end{bmatrix} &= LPF \left( \begin{bmatrix} i_{\alpha h} \\ i_{\beta h} \end{bmatrix} \cos(\omega_h t) \sin(2\omega_h t) \right) \\
 &= LPF \left( \frac{U_h}{\omega_h L_d} \begin{bmatrix} \cos \theta \\ \sin \theta \end{bmatrix} \sin(\omega_h t) \cos(\omega_h t) \sin(2\omega_h t) \right) \\
 &= LPF \left( \frac{2U_h}{\omega_h L_d} \begin{bmatrix} \cos \theta \\ \sin \theta \end{bmatrix} \sin(2\omega_h t) \sin(2\omega_h t) \right) \\
 &= LPF \left( \frac{U_h}{\omega_h L_d} \begin{bmatrix} \cos \theta \\ \sin \theta \end{bmatrix} - \frac{U_h}{\omega_h L_d} \begin{bmatrix} \cos \theta \\ \sin \theta \end{bmatrix} \cos(4\omega_h t) \right) \\
 &= \frac{U_h}{\omega_h L_d} \begin{bmatrix} \cos \theta \\ \sin \theta \end{bmatrix}
 \end{aligned} \tag{10}$$

where *LPF* is low pass filter. From Equation (10), it can be seen that the signal multiplied by the new modulation function consists of a signal containing the rotor's angle position and a signal four times the injection frequency. However, the signal multiplied by the traditional modulation function  $\sin(\omega_h t)$  consists of a signal containing the rotor's angle position and a signal two times the injection frequency. Compared to the traditional modulation function, the frequency of the high-frequency signal increases by two times. Signal separation is easier, and the signal containing rotor position information contains fewer high frequencies, effectively reducing the position estimation error of the rotor. Then, a PLL is introduced to obtain the rotor's angle position. Figure 4 depicts the structure of the PLL, and the structure diagram of the rotor's angle position information extraction process when using the new modulation method is shown in Figure 5.

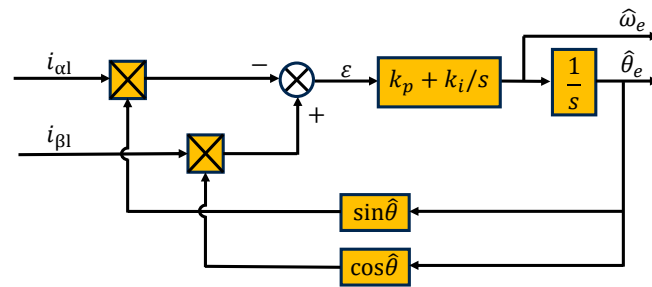


Figure 4. The structure of PLL.

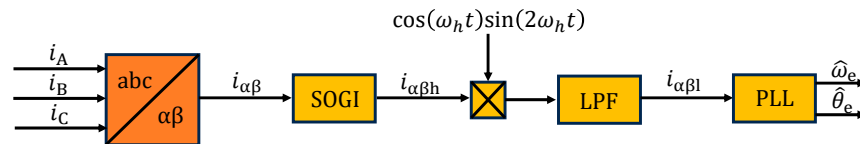


Figure 5. The structure diagram of the position information extraction process.

In Figure 4,  $k_p$  and  $k_i$  are the PI controller's gains of the PLL, respectively.  $\hat{\omega}_e$  and  $\hat{\theta}_e$  are the rotor's estimated electrical velocity and electrical position angle obtained through the PLL, respectively.

In Figure 5,  $i_{\alpha\beta}$  represents the current in the  $d-q$  axis of the motor,  $i_{\alpha\beta h}$  represents the high-frequency current in the  $\alpha-\beta$  axis of the motor after SOGI extraction, and  $i_{\alpha\beta pl}$  represents the current in the  $\alpha-\beta$  axis of the motor that contains rotor's position information after modulation and low-pass filtering.

## 2.2. Improved STSMO Method

When the PMSM operates in medium- and high-speed domains, the SMO can be utilized to estimate the position of the rotor because the back EMF is sufficient. The traditional SMO has defects such as chattering and angle lag, which affect the performance of sensorless control. An improved STSMO with an NPLL is adopted in this section to reduce chattering and improve rotor position estimation accuracy.

The voltage equation of SPMSM under the  $\alpha-\beta$  axis can be written as follows:

$$\begin{bmatrix} u_\alpha \\ u_\beta \end{bmatrix} = R_s \begin{bmatrix} i_\alpha \\ i_\beta \end{bmatrix} + \begin{bmatrix} L_s & 0 \\ 0 & L_s \end{bmatrix} \frac{d}{dt} \begin{bmatrix} i_\alpha \\ i_\beta \end{bmatrix} + \begin{bmatrix} E_\alpha \\ E_\beta \end{bmatrix} \quad (11)$$

where  $u_\alpha$ ,  $u_\beta$  and  $i_\alpha$ ,  $i_\beta$  are the stator voltages and currents in the  $\alpha-\beta$  axis, respectively,  $R_s$  and  $L_s$  are phase resistance and phase inductance, respectively, and  $E_\alpha$  and  $E_\beta$  represent the back EMF, respectively. The back EMF can be expressed as follows:

$$\begin{bmatrix} E_\alpha \\ E_\beta \end{bmatrix} = \omega_e \psi_f \begin{bmatrix} -\sin \theta_e \\ \cos \theta_e \end{bmatrix} \quad (12)$$

where  $\theta_e$  is the electrical angle position of the rotor. The back EMF contains position information of the rotor, which can be obtained by designing an observer. Formula (11) can be rewritten as follows:

$$\frac{d}{dt} \begin{bmatrix} i_\alpha \\ i_\beta \end{bmatrix} = \frac{1}{L_s} \begin{bmatrix} u_\alpha \\ u_\beta \end{bmatrix} - \frac{1}{L_s} \begin{bmatrix} R_s & 0 \\ 0 & R_s \end{bmatrix} \begin{bmatrix} i_\alpha \\ i_\beta \end{bmatrix} - \frac{1}{L_s} \begin{bmatrix} E_\alpha \\ E_\beta \end{bmatrix} \quad (13)$$

Taking the Formula (13) as a reference model, the expression of the designed traditional SMO is as follows:

$$\frac{d}{dt} \begin{bmatrix} \hat{i}_\alpha \\ \hat{i}_\beta \end{bmatrix} = \frac{1}{L_s} \begin{bmatrix} u_\alpha \\ u_\beta \end{bmatrix} - \frac{1}{L_s} \begin{bmatrix} R_s & 0 \\ 0 & R_s \end{bmatrix} \begin{bmatrix} \hat{i}_\alpha \\ \hat{i}_\beta \end{bmatrix} - \frac{1}{L_s} \begin{bmatrix} v_\alpha \\ v_\beta \end{bmatrix} \quad (14)$$

where  $\hat{i}_\alpha$  and  $\hat{i}_\beta$  represent estimated currents,  $v_\alpha$  and  $v_\beta$  are estimated back EMF.  $s = \hat{i} - i$  is chosen as the sliding mode surface. Subtracting Formula (14) from Formula (13), the current error formula is written as follows:

$$\begin{cases} \frac{d\tilde{i}_\alpha}{dt} = -\frac{R_s}{L_s}\tilde{i}_\alpha + \frac{1}{L_s}(E_\alpha - v_\alpha) \\ \frac{d\tilde{i}_\beta}{dt} = -\frac{R_s}{L_s}\tilde{i}_\beta + \frac{1}{L_s}(E_\beta - v_\beta) \end{cases} \quad (15)$$

where  $\tilde{i}_\alpha$  and  $\tilde{i}_\beta$  are the current errors in the  $\alpha - \beta$  axis. The sliding mode control rate of the traditional SMO is as follows:

$$\begin{bmatrix} v_\alpha \\ v_\beta \end{bmatrix} = \begin{bmatrix} k \operatorname{sign}(\tilde{i}_\alpha) \\ k \operatorname{sign}(\tilde{i}_\beta) \end{bmatrix} \quad (16)$$

When the system reaches and moves back and forth on the sliding mode surface,  $v_\alpha = E_\alpha$  and  $v_\beta = E_\beta$ . The back EMF is as follows:

$$\begin{bmatrix} E_\alpha \\ E_\beta \end{bmatrix} = \begin{bmatrix} v_\alpha \\ v_\beta \end{bmatrix} = \begin{bmatrix} k \operatorname{sign}(\tilde{i}_\alpha) \\ k \operatorname{sign}(\tilde{i}_\beta) \end{bmatrix} \quad (17)$$

The basic model of the STSMO can be written as [36]:

$$\begin{cases} \frac{d\hat{x}_1}{dt} = -k_1 |\tilde{x}_1|^{\frac{1}{2}} \operatorname{sign}(\tilde{x}_1) + \hat{x}_2 + \rho_1 \\ \frac{d\hat{x}_2}{dt} = -k_2 \operatorname{sign}(\tilde{x}_1) + \rho_2 \end{cases} \quad (18)$$

where  $\hat{x}_1$  and  $\hat{x}_2$  represent estimated state variables of the system,  $\tilde{x}_1$  represents the error between the actual state variable and the estimated state variable,  $k_1$  and  $k_2$  are sliding mode coefficients,  $k_1$  affects the rate of convergence of the STSMO, and the value of  $k_2$  is related to the effect of suppressing chattering. The larger  $k_1$ , the faster the convergence rate; the larger  $k_2$ , the better the effect of suppressing chattering.  $\rho_1$  and  $\rho_2$  are disturbance terms.

On the basis of the Lyapunov stability theorem, the STSMO is stable and can converge to the sliding mode surface in a limited time.  $\rho_1$ ,  $\rho_2$ ,  $k_1$ , and  $k_2$  in Equation (18) need to satisfy the following conditions [37]:

$$\begin{cases} \rho_1 \leq \delta |\tilde{x}_1|^{\frac{1}{2}} \\ \rho_2 = 0 \end{cases} \quad (19)$$

$$\begin{cases} k_1 > 2\delta \\ k_2 > k_1 \frac{5\delta k_1 + 4\delta^2}{2(k_1 - 2\delta)} \end{cases} \quad (20)$$

where  $\delta$  is a constant greater than 0.

Replacing the state variables with  $\hat{i}_\alpha$ ,  $\hat{i}_\beta$ ,  $\tilde{i}_\alpha$ , and  $\tilde{i}_\beta$ , Formula (18) can be rewritten as follows:

$$\begin{cases} \frac{d\hat{i}_\alpha}{dt} = -k_1 |\tilde{i}_\alpha|^{\frac{1}{2}} \operatorname{sign}(\tilde{i}_\alpha) - \int k_2 \operatorname{sign}(\tilde{i}_\alpha) dt + \rho(\hat{i}_\alpha) \\ \frac{d\hat{i}_\beta}{dt} = -k_1 |\tilde{i}_\beta|^{\frac{1}{2}} \operatorname{sign}(\tilde{i}_\beta) - \int k_2 \operatorname{sign}(\tilde{i}_\beta) dt + \rho(\hat{i}_\beta) \end{cases} \quad (21)$$

Formula (21) is the STSMO model of the PMSM, and the disturbance terms can be expressed as follows [38]:

$$\begin{cases} \rho(\hat{i}_\alpha) = \frac{1}{L_s}u_\alpha - \frac{R_s}{L_s}\hat{i}_\alpha \\ \rho(\hat{i}_\beta) = \frac{1}{L_s}u_\beta - \frac{R_s}{L_s}\hat{i}_\beta \end{cases} \quad (22)$$

where  $\rho(\hat{i}_\alpha)$  and  $\rho(\hat{i}_\beta)$  are the disturbance terms of estimated currents in the  $\alpha - \beta$  axis of the motor, respectively.

From Formula (20), the following conditions for system stability need to be satisfied:

$$\begin{cases} \frac{1}{L_s}u_\alpha - \frac{R_s}{L_s}\hat{i}_\alpha \leq \delta \left| \hat{i}_\alpha \right|^{\frac{1}{2}} \\ \frac{1}{L_s}u_\beta - \frac{R_s}{L_s}\hat{i}_\beta \leq \delta \left| \hat{i}_\beta \right|^{\frac{1}{2}} \end{cases} \quad (23)$$

From Equations (13) and (21), the error of the current is written as follows:

$$\begin{cases} \frac{d\tilde{i}_\alpha}{dt} = -\frac{R_s}{L_s}\tilde{i}_\alpha - k_1 \left| \tilde{i}_\alpha \right|^{\frac{1}{2}} \text{sign}(\tilde{i}_\alpha) - \int k_2 \text{sign}(\tilde{i}_\alpha) dt + \frac{E_\alpha}{L_s} \\ \frac{d\tilde{i}_\beta}{dt} = -\frac{R_s}{L_s}\tilde{i}_\beta - k_1 \left| \tilde{i}_\beta \right|^{\frac{1}{2}} \text{sign}(\tilde{i}_\beta) - \int k_2 \text{sign}(\tilde{i}_\beta) dt + \frac{E_\beta}{L_s} \end{cases} \quad (24)$$

The estimated back EMF value is approximately equivalent to the actual back EMF value when the observer reaches and moves back and forth on the sliding mode surface. The back EMF is expressed as follows:

$$\begin{cases} E_\alpha = L_s(k_1 \left| \tilde{i}_\alpha \right|^{\frac{1}{2}} \text{sign}(\tilde{i}_\alpha) + \int k_2 \text{sign}(\tilde{i}_\alpha) dt) \\ E_\beta = L_s(k_1 \left| \tilde{i}_\beta \right|^{\frac{1}{2}} \text{sign}(\tilde{i}_\beta) + \int k_2 \text{sign}(\tilde{i}_\beta) dt) \end{cases} \quad (25)$$

Since the discontinuous sign function will lead to chattering, to improve the observer performance and suppress chattering, the continuous hyperbolic tangent function is chosen as the switch function instead of the sign function in this paper, whose expression is as follows:

$$h(s) = \frac{e^{ms} - e^{-ms}}{e^{ms} + e^{-ms}} \quad (26)$$

where  $m > 0$ , which is utilized to control the thickness of the boundary layer. The smaller  $m$  is, the larger the boundary layer is, and the better the chattering repression effect is, but it will reduce control accuracy. The larger  $m$  is, the smaller the boundary layer is, and the control accuracy is better, but the system chattering will also increase. Therefore, selecting an appropriate  $m$  can achieve system control accuracy while also suppressing system chattering. The system back EMF is written as follows:

$$\begin{cases} E_\alpha = L_s(k_1 \left| \tilde{i}_\alpha \right|^{\frac{1}{2}} h(\tilde{i}_\alpha) + \int k_2 h(\tilde{i}_\alpha) dt) \\ E_\beta = L_s(k_1 \left| \tilde{i}_\beta \right|^{\frac{1}{2}} h(\tilde{i}_\beta) + \int k_2 h(\tilde{i}_\beta) dt) \end{cases} \quad (27)$$

The arctangent function method is utilized to obtain the position and speed of the rotor of PMSM in traditional SMO, which can be expressed as follows:

$$\begin{cases} \hat{\omega}_e = \frac{d\hat{\theta}_e}{dt} \\ \hat{\theta}_e = -\arctan\left(\frac{e_\alpha}{e_\beta}\right) \end{cases} \quad (28)$$

When the observer moves up and down on the sliding mode surface, the back EMF contains discontinuous high-frequency switching noise signals; using the arctangent function method leads to serious chattering, leading to inaccuracies in determining the rotor's position angle. To enhance estimation accuracy, a novel phase-locked loop (NPLL) is devised in this paper to extract the estimated back electromotive force (EMF) and precisely ascertain the rotor's position angle. The structure of the NPLL is shown in Figure 6.

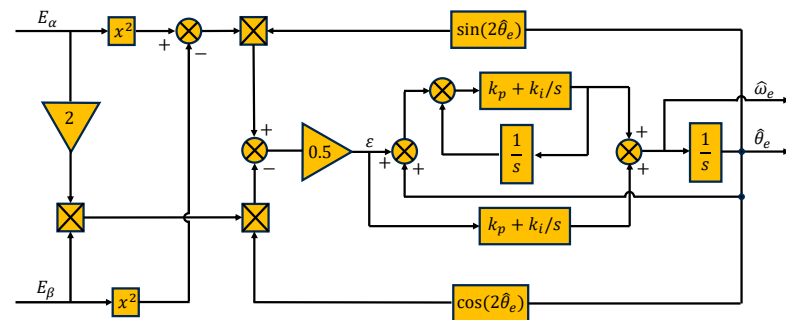


Figure 6. The structure of the NPLL.

From Figure 6, the position error  $\varepsilon$  can be expressed as follows:

$$\begin{aligned} \varepsilon &= \frac{(E_\alpha^2 - E_\beta^2)}{2} \sin(2\hat{\theta}_e) - E_\alpha E_\beta \cos(2\hat{\theta}_e) \\ &= (\omega_e \psi_f)^2 \sin(\theta_e) \cos(\theta_e) \cos(2\hat{\theta}_e) \\ &\quad + \frac{(\omega_e \psi_f)^2 \sin(2\hat{\theta}_e)}{2} (\sin^2(\theta_e) - \cos^2(\theta_e)) \\ &= (\omega_e \psi_f)^2 \left( \frac{\sin(2\theta_e) \cos(2\hat{\theta}_e)}{2} - \frac{\cos(2\theta_e) \sin(2\hat{\theta}_e)}{2} \right) \\ &= \frac{1}{2} (\omega_e \psi_f)^2 \sin(2(\theta_e - \hat{\theta}_e)) \approx (\omega_e \psi_f)^2 (\theta_e - \hat{\theta}_e) \end{aligned} \quad (29)$$

The closed-loop transfer function of the NPLL is written as follows:

$$G_{\text{NPLL}}(s) = \frac{\hat{\theta}_e(s)}{\theta_e(s)} = \frac{2k_p s^3 + (2k_i + k_p^2)s^2 + 2k_p k_i s + k_i^2}{(s^2 + k_p s + k_i)^2} \quad (30)$$

According to [39], Formula (30) can be rewritten as follows:

$$G_{\text{NPLL}}(s) = \frac{\hat{\theta}_e(s)}{\theta_e(s)} = \frac{4\zeta \omega_n s^3 + (4\zeta^2 + 2)\omega_n^2 s^2 + 4\zeta \omega_n^3 s + \omega_n^4}{(s^2 + 2\zeta \omega_n s + \omega_n^2)^2} \quad (31)$$

Comparing Formula (30) with (31), parameters  $k_p$  and  $k_i$  can be designed as follows:

$$\begin{cases} k_p = 2\zeta \sqrt{k_i} \\ k_i = \omega_n^2 \end{cases} \quad (32)$$

where  $\zeta$  is the damping factor, which can affect the dynamic response and overshoot of the system,  $\omega_n$  is the natural frequency, which determines the convergence time and noise suppression effect of the system. The larger the  $\zeta$ , the slower the dynamic response, and the smaller the overshoot; the larger the  $\omega_n$ , the faster the convergence time, the larger the noise bandwidth, and the worse the noise suppression effect. In this article,  $\zeta$  and  $\omega_n$

are chosen as 0.707 and 50 rad/s. According to the Routh–Hurwitz stability theorem, the conditions for the stability of the NPLL need to satisfy  $\zeta > 0$  and  $\omega_n > 0$  [39].

### 2.3. Transition between Low Speed and Medium and High Speeds

The back EMF of the PMSM is negligible in the low-speed domain, resulting in large position errors when estimated using the SMO. To address this challenge, the new HFPVI method is employed for low speeds, while the SMO is employed in the medium-speed domain and high-speed domain in this paper. Due to the use of different estimation strategies to make the motor smoothly transit from the low-speed range to the medium-to-high-speed domain, a new exponential weighting function  $\alpha$  is designed in this paper to achieve smooth switching between the transition process, which can be expressed as follows:

$$\alpha = \begin{cases} 1 & \hat{n} \leq n_1 \\ \frac{e^{\frac{n_2 - \hat{n}}{n_2 - n_1}} - 1}{e - 1} & n_1 < \hat{n} < n_2 \\ 0 & \hat{n} > n_2 \end{cases} \quad (33)$$

$$\begin{cases} \hat{\theta} = \alpha \hat{\theta}_l + (1 - \alpha) \hat{\theta}_h \\ \hat{\omega} = \alpha \hat{\omega}_l + (1 - \alpha) \hat{\omega}_h \end{cases} \quad (34)$$

where  $\hat{\theta}_l$  and  $\hat{\omega}_l$  are the rotor's angle position and velocity estimated by the proposed new HFPVI method, respectively,  $\hat{\theta}_h$  and  $\hat{\omega}_h$  are the rotor's angle position and velocity obtained by the improved STSMO, respectively,  $n_1$  is the speed value to start the switching, and  $n_2$  is the speed value to end the switching;  $n_1$  can be chosen as about 10% of the motor's rated speed. When  $\hat{n} \leq n_1$ , the position and velocity of the rotor are obtained by the proposed new HFPVI method. When  $n_1 < \hat{n} < n_2$ , the rotor's position and velocity are obtained by the proposed new HFPVI method and the improved STSMO; when  $\hat{n} > n_2$ , the rotor's position and velocity are obtained by the improved STSMO. The weighted switching function curve is depicted in Figure 7.

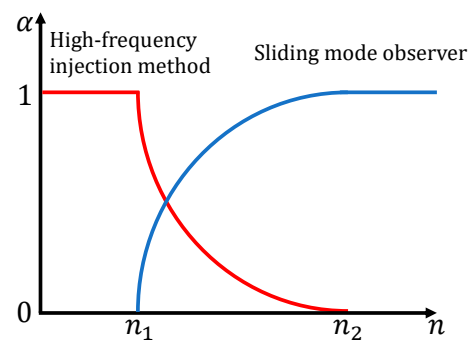


Figure 7. Weighted switching function curve.

### 3. Simulation Results

To confirm that the control strategies are effective, simulation models are constructed in Simulink. The FOC control strategy is adopted in this article and  $i_{dref}$  is set to 0. The reference angular velocity  $\omega_{ref}$  is the control input; the estimated electrical angle position  $\hat{\theta}_e$  and electrical angular velocity  $\hat{\omega}_e$  are the control outputs. The main parameters of the SPMSM are shown in Table 1. Tables 2 and 3 provide hyperparameters of the proposed new HFPVI method and improved STSMO in simulation, respectively.



**Table 1.** Basic parameters of the SPMSM.

Rated power (kW)	1.5
Rated speed (rpm)	2500
Rated torque (N·m)	6
Stator inductance (mH)	1.975
Stator resistance ( $\Omega$ )	0.64
Pole pairs	4

**Table 2.** Hyperparameters of the proposed new HFPVI method.

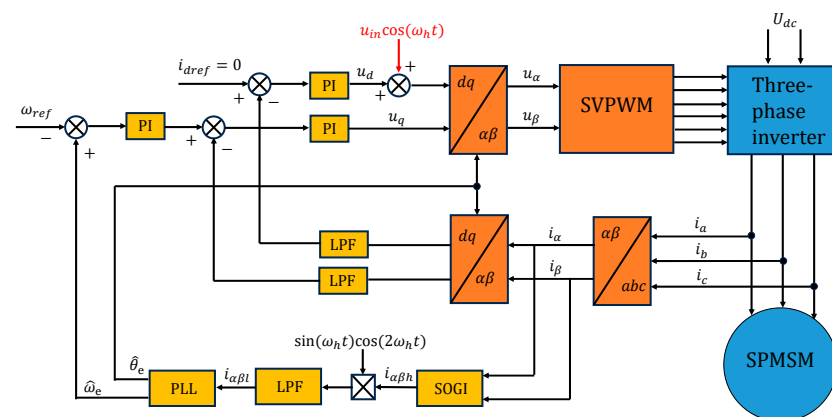
SOGI	$K = 0.1$
PLL	$k_p = 50, k_i = 600$

**Table 3.** Hyperparameters of the improved STSMO.

STSMO	$k_1 = 50, k_2 = 2500$
NPLL	$k_p = 50, k_i = 2500$

### 3.1. Sensorless Control Based on the Proposed HFPVI Method

The model diagram of the proposed new HFPVI method for SPMSM is depicted in Figure 8. In Figure 8,  $\omega_{ref}$  represents the reference angular velocity and PI stands for the PI controller in the d–q axis current loop. High-frequency voltage is applied to the estimated d-axis. The high-frequency current signal, which includes the angle position information of the rotor, can be extracted in the  $\alpha$ – $\beta$  axis by SOGI. Subsequently, the high-frequency current is multiplied by a modulated signal  $\cos(\omega_h t)\sin(2\omega_h t)$ , filtered by a LPF, and eventually, the estimated rotor's position of the SPMSM is determined through a PLL. The amplitude and frequency of the injected high-frequency cosine voltage are 0.4 V and 1 kHz, respectively. The reference speed is set at 200 rpm.

**Figure 8.** Block diagram of the proposed new HFPVI method.

#### 3.1.1. Simulation Results of the Proposed New HFPVI without Load

Figure 9 depicts the corresponding simulation results of the proposed new HFPVI without load. As depicted in Figure 9, the motor runs from 0 to 200 rpm without load. The error of position during acceleration is less than 0.25 rad (14 elc-deg) when the motor runs steadily at 200 rpm; this is approximately 0.025 rad (1.4 elc-deg).

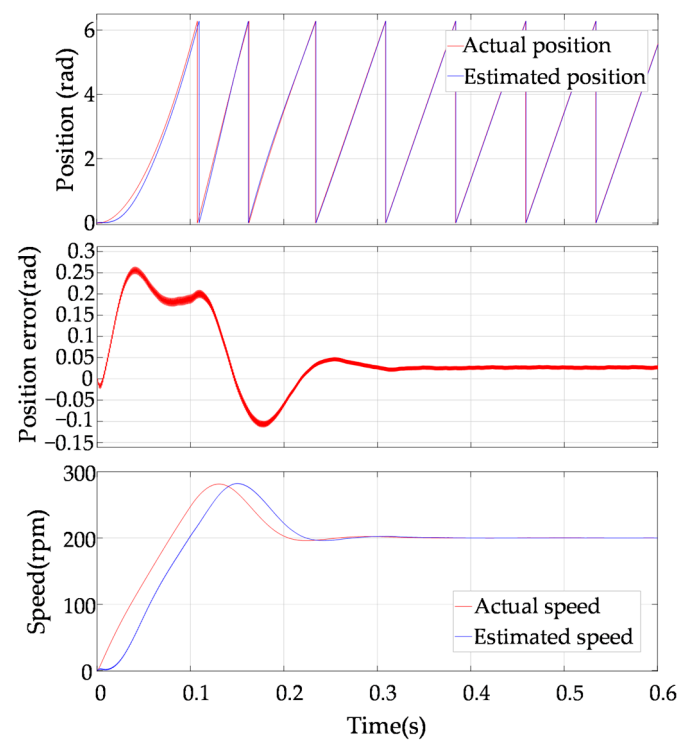


**Figure 9.** Simulation results of the proposed new HFPVI method under no-load conditions.

### 3.1.2. Simulation Results of the Proposed New HFPVI with Constant Load

Figure 10 depicts the corresponding results of the new HFPVI's simulation with a constant load torque of 2 N·m. As depicted in Figure 10, the motor runs from 0 to 200 rpm under a constant load of 2 N·m. The position error during acceleration is less than 0.2 rad (11.5 elc-deg). When the motor is running stably, the error of position estimated by the new HFPVI is approximately 0.04 rad (2.3 elc-deg).

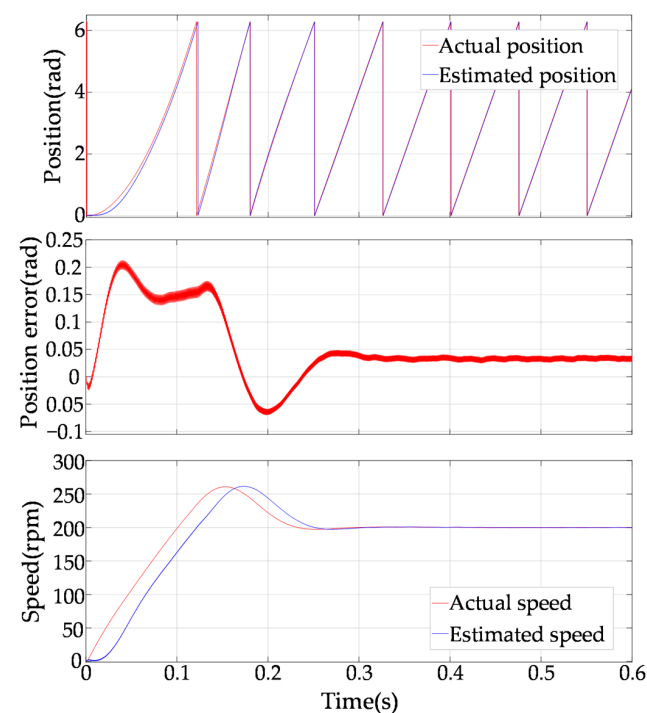


**Figure 10.** Simulation results of the proposed new HFPVI method under a constant load torque of 2 N·m.

### 3.1.3. Simulation Results of the Proposed New HFPVI with Sudden Load

Figure 11 depicts the corresponding results of the simulation of the new HFPVI when the motor is suddenly loaded with 2 N·m. As depicted in Figure 11, the motor runs steadily at 100 rpm, and a load torque of 2 N·m is suddenly applied to the motor at 0.4 s. When the motor runs stably, the error of position estimated by the new HFPVI is about 0.02 rad (1.1 elc·deg). When the motor is loaded, the error of position is up to 0.06 rad (3.4 elc·deg).

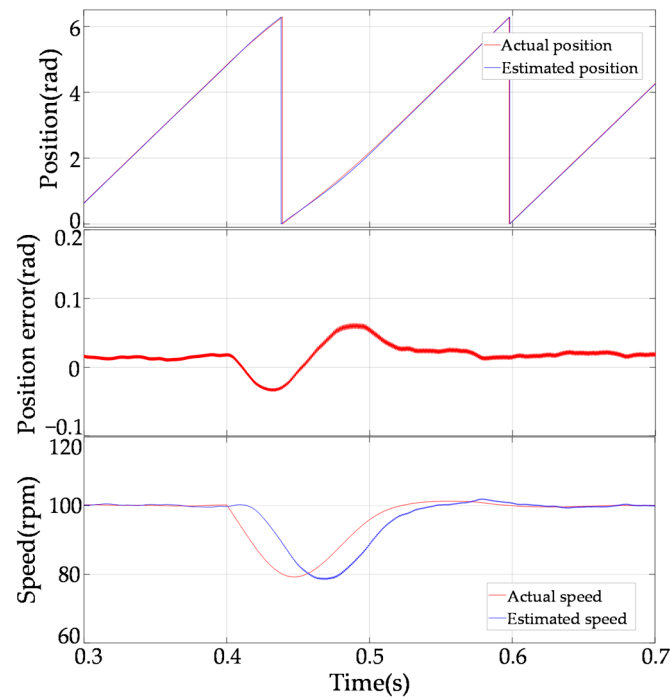


**Figure 11.** Simulation results of the proposed new HFPVI with a sudden loading of 2 N·m.

### 3.2. Sensorless Control Based on Improved STSMO Method

The improved STSMO sensorless control model is depicted in Figure 12, and related comparative simulations and analyses are performed to verify the effectiveness and superiority.

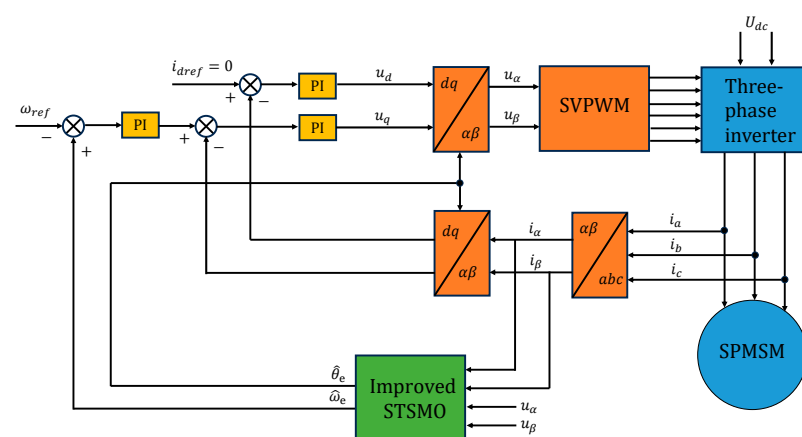


**Figure 12.** Improved STSMO sensorless control model diagram.

The simulation comparison between the traditional SMO and the improved STSMO is conducted to verify that the improved STSMO reduces chattering to a certain extent and enhances the rotor position estimation accuracy.

### 3.2.1. Simulation Results of the Traditional SMO and the Improved STSMO without Load

Figure 13 depicts the results of the comparative simulation of the traditional SMO and the improved STSMO without load. The initial reference speed is determined as 300 rpm, and the reference speed is adjusted to 800 rpm at 0.1 s. As depicted in Figure 13a, the position error estimated by the traditional SMO is approximately 0.07 rad (4 elc-deg); the position error converges slowly when using the traditional PLL, and the position error has an increase of 0.15 rad (8.6 elc-deg) during the acceleration process. The chattering phenomenon is inevitable owing to the sign function. As depicted in Figure 13b, the chattering is suppressed when the improved STSMO is adopted, and the position error is less than 0.02 (1.15 elc-deg) rad and is close to 0.0025 rad (0.14 elc-deg) when the motor runs steady. The position error converges very fast when the NPLL is adopted, and the position error decreases during the acceleration process.

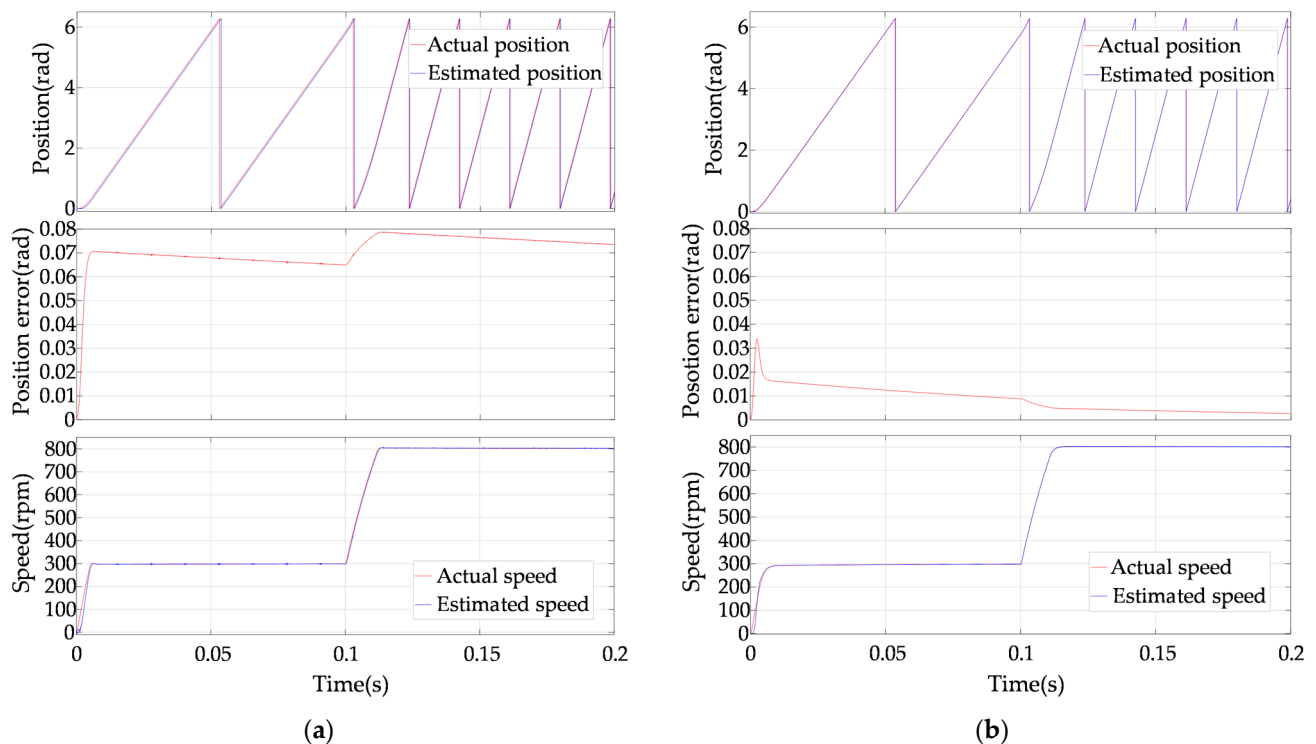


**Figure 13.** Comparative simulation results of the traditional SMO and the improved STSMO without load. (a) Traditional SMO; (b) improved STSMO.

### 3.2.2. Comparative Simulation Results of the Traditional SMO and the Improved STSMO with Constant Load

Figure 14 depicts the results of the comparative simulation of the traditional SMO and the improved STSMO under a constant load torque of 2 N·m. The initial reference speed is set at 300 rpm; the reference speed is adjusted to 800 rpm at 0.1 s. As depicted in Figure 14a, a chattering phenomenon exists when using traditional SMO. The position error of the traditional SMO is about 0.07 rad (4 elc-deg), and the position error converges slowly when using the traditional PLL; the position error has an increase of 0.15 rad (8.6 elc-deg) during the acceleration process. As depicted in Figure 14b, the chattering is suppressed when the improved STSMO is adopted. The position error converges very fast when the NPLL is adopted, and the position error increases by 0.005 rad (0.29 elc-deg) during the acceleration and is close to 0 rad when the motor runs steady.

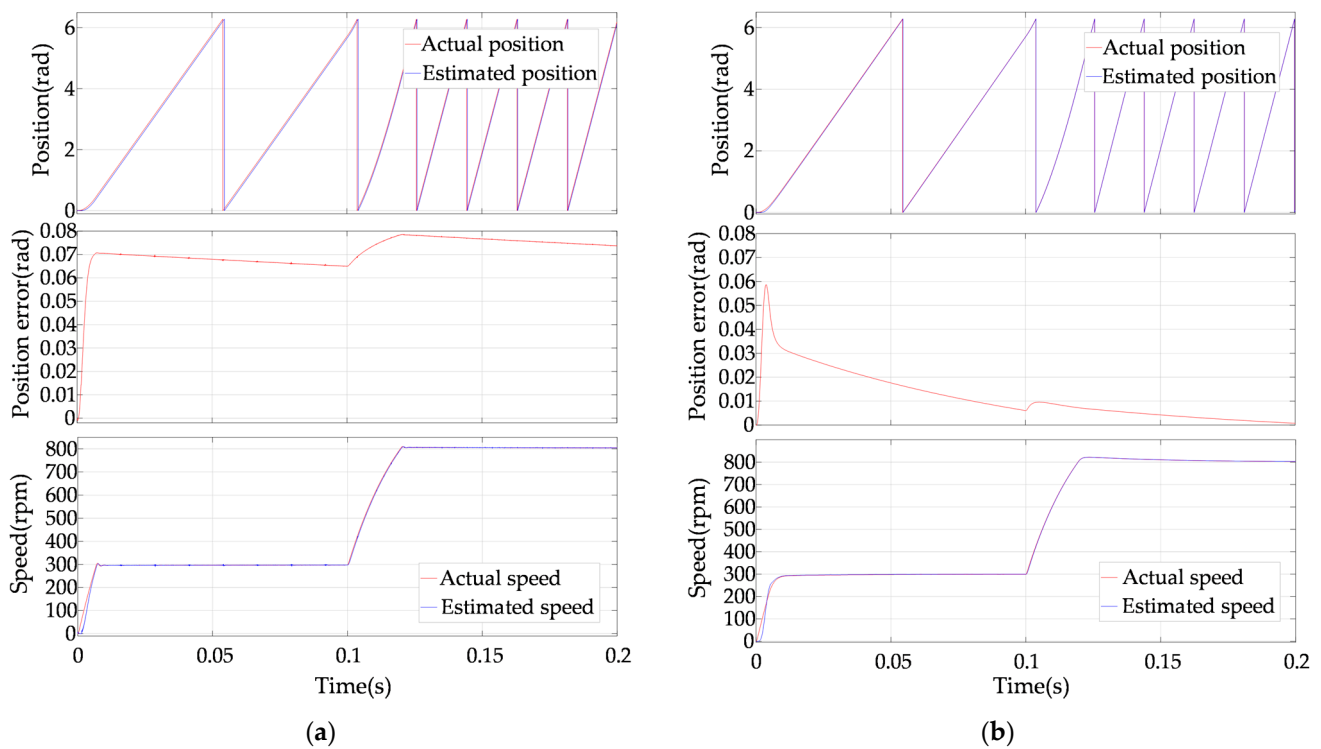


**Figure 14.** Comparative simulation results of the traditional SMO and the improved STSMO with a constant load torque of 2 N·m. (a) Traditional SMO; (b) improved STSMO.

### 3.2.3. Comparative Simulation Results of the Traditional SMO and the Improved STSMO with Sudden Load

Figure 15 depicts the results of the comparative simulation of the traditional SMO and the improved STSMO with a sudden load torque of 2 N·m. As depicted in Figure 15a, the motor obviously suffers from chattering. The position error is around 0.06 rad (3.4 elc-deg), and the speed drops by 18 rpm when the motor is loaded. As depicted in Figure 15b, the chattering is reduced significantly when the improved STSMO is employed. When the motor is suddenly loaded, the error of the rotor's position is less than 0.01 rad (0.57 elc-deg), and the speed drops by 15 rpm. Compared with traditional SMO, the estimation accuracy of the rotor's position is enhanced, and chattering is reduced.

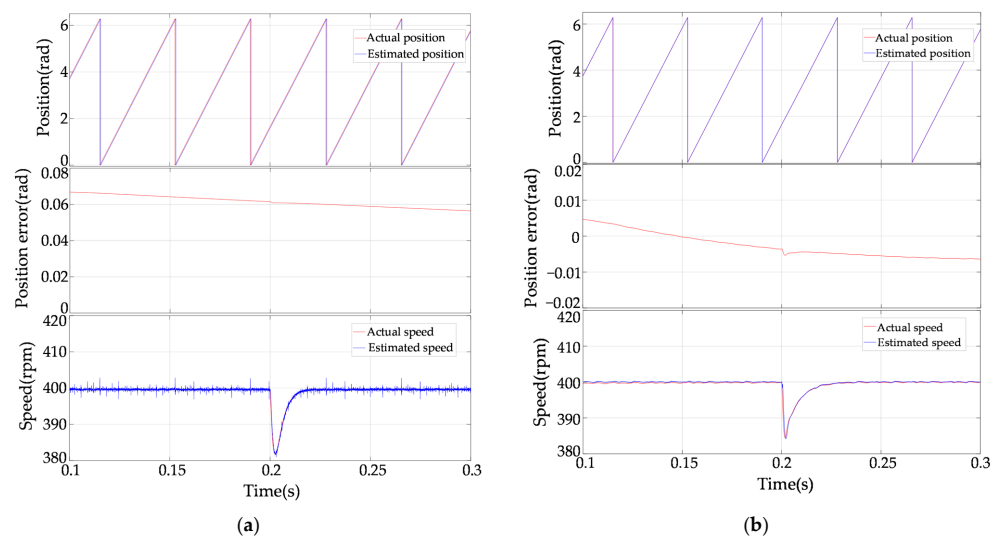


**Figure 15.** Comparative simulation results of the traditional SMO and the improved STSMO with a sudden load torque of 2 N·m. (a) Traditional SMO; (b) improved STSMO.

### 3.3. Transition from Low Speed to Medium and High Speeds

The model diagram of sensorless control in a wide-speed range is depicted in Figure 16, and related simulations are conducted to validate its effectiveness. When the specified speed is below 300 rpm, the proposed new HFPVI method is utilized to determine the rotor position. For speeds exceeding 400 rpm, an improved STSMO is utilized for rotor position estimation. In the speed domain between 300 and 400 rpm, the rotor's position is provided by both the new HFPVI method and the improved STSMO. A constant load torque of 2 N·m is applied in the simulations.

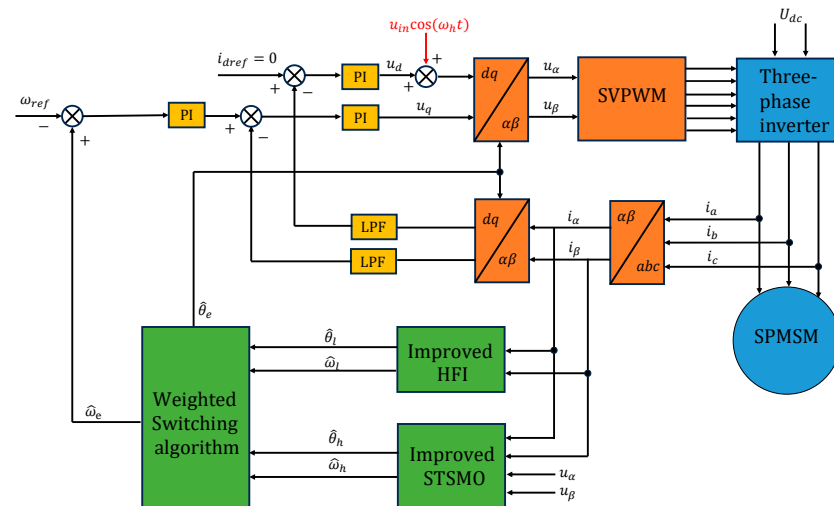


**Figure 16.** Wide-speed range sensorless control model diagram.

Figure 17 depicts the simulation results of sensorless control in a wide-speed range. The motor reference speed is determined as 800 rpm. In the process of transition from 300 rpm to 400 rpm, the switching is relatively smooth, and there is no fluctuation.

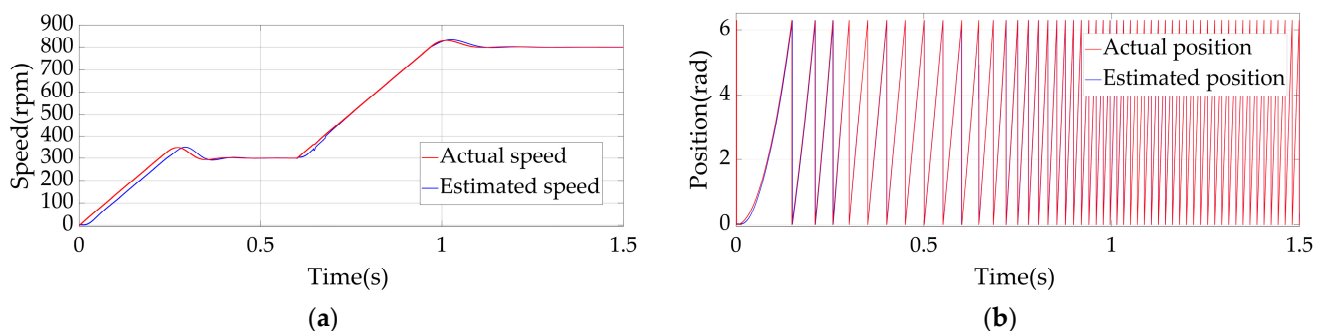


**Figure 17.** Simulation results of wide-speed range sensorless control. (a) Speed; (b) position.

## 4. Experimental Results

Experiments were carried out to validate the effectiveness and superiority of the proposed new HFPVI and improved STSMO on the platform, as shown in Figure 18. The RTU-BOX serves as a real-time digital controller, with the inverter's switching frequency set at 10 kHz and a dead time of 0.1  $\mu$ s. The test motor used is a 1.5 kW SPMSM, and the key parameters of this motor are detailed in Table 1. The incremental encoder resolution is 2500 bits, while the load motor is a 4.5 kW SPMSM controlled by a 220 V servo drive.



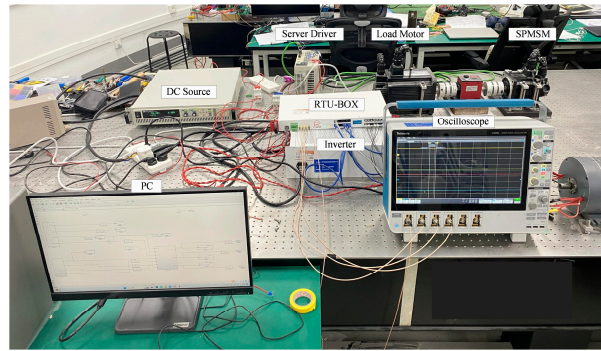


**Figure 18.** Experimental platform.

#### 4.1. Experimental Tests Based on the Proposed New HFPVI Method

##### 4.1.1. Experimental Results of the Proposed New HFPVI without Load

Figure 19 depicts the experimental results of the proposed new HFPVI method under no-load conditions. The initial reference speed is determined as 50 rpm, and it is adjusted to 200 rpm at 1 s. The proposed new HFPVI method can accurately track the rotor position with a position error of about 0.05 rad (2.87 elc-deg), a speed error of less than 20 rpm during acceleration, and less than 10 rpm when the motor runs stably.

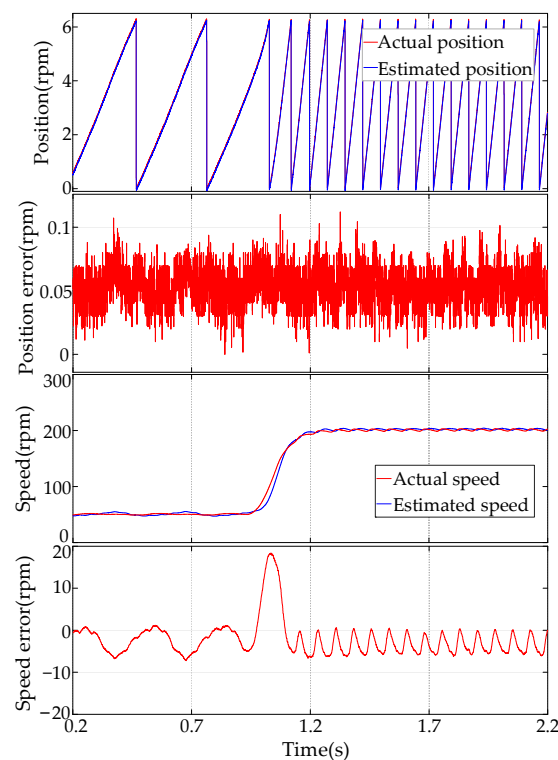


**Figure 19.** Experimental results of the proposed new HFPVI method without load.

##### 4.1.2. Experimental Results of the New HFPVI with Constant Load

Figure 20 illustrates the results of the experiment of the proposed new HFPVI method under a constant load torque of 2 N·m. The initial reference speed is determined as 50 rpm, and at 1.2 s, it is adjusted to 200 rpm. The position error is around 0.06 rad (3.44 elc-deg), with the speed error during acceleration being less than 20 rpm. These experimental findings validate the effectiveness of the proposed new HFPVI method.

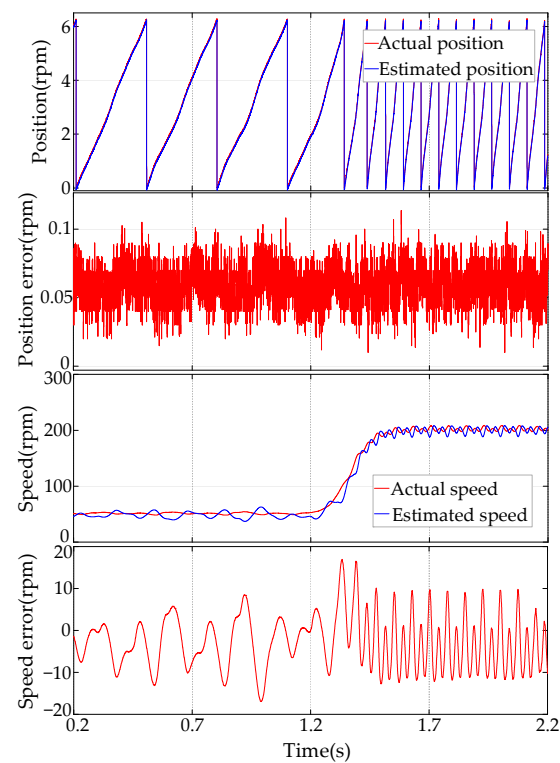


**Figure 20.** Experimental results of the proposed new HFPVI method under a constant load torque of 2 N·m.

#### 4.2. Comparative Experiments of the Traditional SMO and the Improved STSMO Method

The comparison tests between the traditional SMO and the improved STSMO method are illustrated in Figures 21–23.

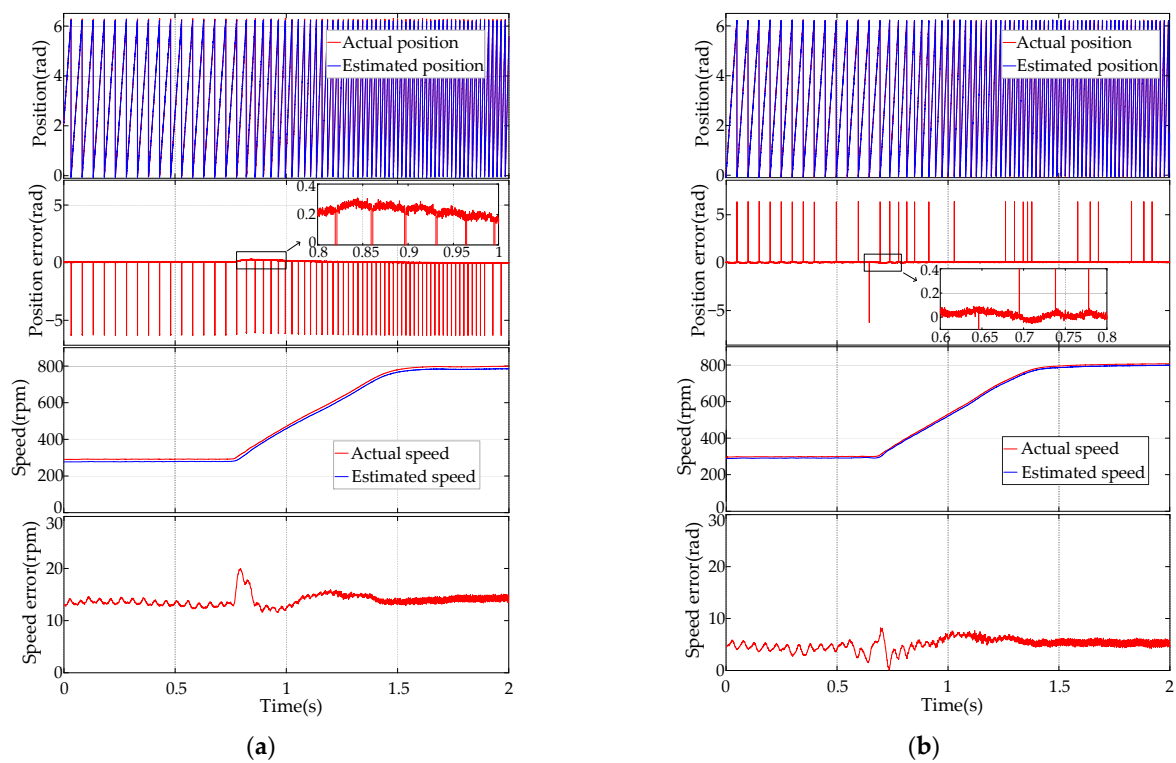


**Figure 21.** Comparative experimental results of the traditional SMO and the improved STSMO without load. (a) Traditional SMO; (b) improved STSMO.

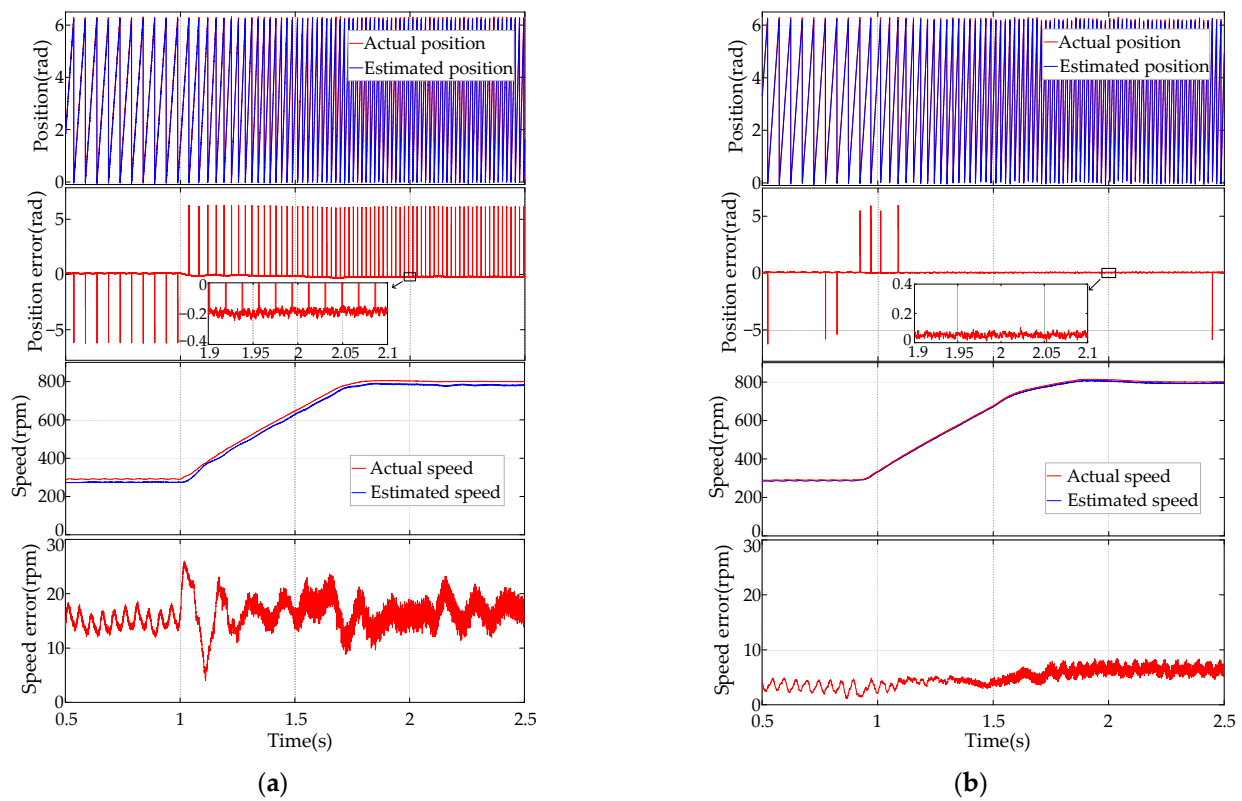


**Figure 22.** Comparative experimental results of the traditional SMO and the improved STSMO with a constant load torque of 2 N·m. (a) Traditional SMO; (b) improved STSMO.

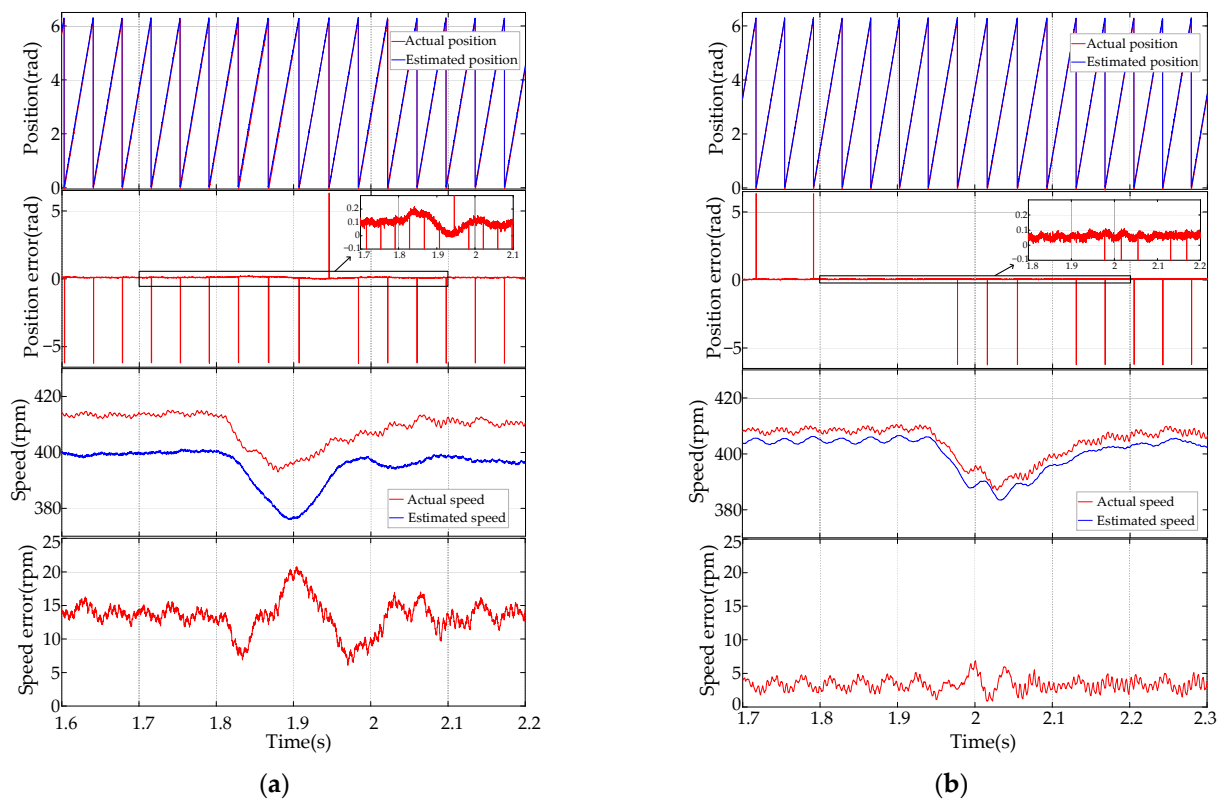


**Figure 23.** Comparative experimental results of the traditional SMO and the improved STSMO with a sudden load torque of 2 N·m. (a) Traditional SMO; (b) improved STSMO.

#### 4.2.1. Comparative Experimental Results of the Traditional SMO and the Improved STSMO without Load

Figure 21 illustrates the results of the comparative experiments of the traditional SMO and the improved STSMO without any load. In Figure 21a, the initial reference speed is determined as 300 rpm and adjusted to 800 rpm at 0.75 s. While the motor operates steadily at 300 rpm, the position error of the traditional SMO is approximately 0.05 rad (2.9 elc-deg). However, during acceleration, the position error increases to as high as 0.28 rad (16 elc-deg), with slow convergence when using the traditional PLL. The speed error estimated by the traditional SMO is approximately 13 rpm during stable operation and can reach up to 20 rpm during acceleration. In Figure 21b, the initial reference speed is determined as 300 rpm and adjusted to 800 rpm at 0.65 s. The position error of the improved STSMO remains close to 0 rad during stable motor operation. When utilizing the NPLL, the position error only experiences a small increase of 0.08 rad (4.6 elc-deg) during acceleration. The speed error estimated by the improved STSMO is approximately 5 rpm during stable operation and does not exceed 10 rpm during acceleration. Table 4 shows the experimental results of the two methods without load.

**Table 4.** Comparative experimental results of the traditional SMO and the improved STSMO without load.

Methods	Traditional SMO	Improved STSMO
Steady-state position error	0.05 rad (2.9 elc-deg)	Near 0
Maximum position error during acceleration	0.28 rad (16 elc-deg)	0.08 rad (4.6 elc-deg)
Maximum speed error	20 rpm	8 rpm

#### 4.2.2. Comparative Experimental Results of the Traditional SMO and the Improved STSMO under Constant Load

Figure 22 illustrates the results of comparative experiments of the traditional SMO and the improved STSMO under a constant load torque of 2 N·m. The initial reference speed is determined as 300 rpm; at 1 s, the reference speed is adjusted to 800 rpm. In Figure 22a, the position error of the traditional SMO is approximately 0.2 rad (11.5 elc-deg) when the motor operates steadily at 800 rpm, and it increases to about 0.25 rad (14.3 elc-deg) during the acceleration process when using the traditional PLL. The speed error estimated by the traditional SMO is around 15 rpm during stable operation and can reach up to 25 rpm during acceleration. In Figure 22b, the position error of the improved STSMO is approximately 0.05 rad (2.9 elc-deg) during stable motor operation, with the position error only increasing by 0.1 rad (5.8 elc-deg) during acceleration when the NPLL is employed. The speed error of the improved STSMO is approximately 5 rpm during stable operation and remains below 10 rpm during acceleration. Table 5 shows the experimental results of the two methods with constant load.

**Table 5.** Comparative experimental results of the traditional SMO and the improved STSMO with constant load.

Methods	Traditional SMO	Improved STSMO
Steady-state position error	0.2 rad (11.5 elc-deg)	0.05 rad (2.9 elc-deg)
Maximum position error during acceleration	0.25 rad (14.3 elc-deg)	0.1 rad (5.8 elc-deg)
Maximum speed error	25 rpm	8 rpm

#### 4.2.3. Comparative Experimental Results of the Traditional SMO and the Improved STSMO with Sudden Load

Figure 23 illustrates the results of comparative experiments of the traditional SMO and the improved STSMO under a sudden load torque of 2 N·m. The motor operates steadily at 400 rpm. In Figure 23a, when the motor runs consistently, the position error of the traditional SMO is approximately 0.1 rad (5.7 elc-deg) with a speed error of about 15 rpm. However, when the motor is suddenly loaded, the position error increases to as high as 0.2 rad (11.5 elc-deg), and the speed error rises to around 21 rpm. In Figure 23b, the position error of the improved STSMO is about 0.05 rad (2.9 elc-deg) during stable motor operation. The position error reaches up to 0.1 rad (5.8 elc-deg) when the motor is suddenly loaded. The speed error of the improved STSMO is approximately 4 rpm during steady operation and remains below 7 rpm when the load is abruptly added to the motor. Table 6 shows the experimental results of the two methods with sudden load.

**Table 6.** Comparative experiments of the traditional SMO and the improved STSMO with sudden load.

Methods	Traditional SMO	Improved STSMO
Steady-state position error	0.1 rad (5.7 elc-deg)	0.05 rad (2.9 elc-deg)
Maximum position error	0.2 rad (11.5 elc-deg)	0.1 rad (5.8 elc-deg)
Maximum speed error	21 rpm	4 rpm

## 5. Conclusions

In this paper, the research work on sensorless control of SPMSM in a wide-speed domain is as follows:

- (1) A new HFPVI method is proposed for SPMSMs in a low-speed domain that does not rely on motor saliency. Then, during the modulation process, a SOGI is utilized instead of traditional BPF, and a new modulation signal is designed to separate frequencies more easily.
- (2) An improved STSMO method is proposed for the medium- and high-speed domains. The STSMO and a continuous hyperbolic tangent function are employed to suppress chattering, and an NPLL is adopted to accurately obtain rotor position information.
- (3) An exponential weighted switching function is designed to achieve smooth switching between the low-speed domain and the medium- and high-speed domains.
- (4) The effectiveness of the new HFPVI and the improved STSMO have been verified by the simulations and experimental tests on the RTU-BOX platform under different operating conditions, which provide the foundation for practical applications in the industrial field.
- (5) In this paper, we only conducted experiments with a sudden load of 2 N·m and a constant load of 2 N·m applied to the motor. In the future, we intend to evaluate the anti-disturbance performance of the methods proposed in this paper across a broader range of different loads. For example, the load is configured to the rated load torque of the motor. Furthermore, we plan to improve SOGI and STSMO to improve the rotor position estimation accuracy. This future research can potentially enhance the robustness and effectiveness of the methods across an even broader spectrum of operational conditions.

**Author Contributions:** Y.C. wrote the paper and implemented simulations and experiments; X.L. and X.W. supervised all processes and checked the paper format. All authors have read and agreed to the published version of the manuscript.



**Funding:** This work was supported by the Guangxi Natural Science Foundation (grant number 2022GXNSFBA035622), the Guangxi Science and Technology Plan Project (grant number AD23026124), the Guangxi Science and Technology Major Program (grant number AA23023012), the Guangxi Science and Technology Major Program (grant number AA23073019), and the Guangxi Key Research and Development Plan (grant number AB23049006).

**Data Availability Statement:** Data are contained within the article.

**Conflicts of Interest:** The authors declare no conflicts of interest.

## References

1. Xu, D.; Wang, B.; Zhang, G.; Wang, G.; Yu, Y. A review of sensorless control methods for AC motor drives. *CES Trans. Electr. Mach. Syst.* **2018**, *2*, 104–115. [\[CrossRef\]](#)
2. Flieh, H.M.; Slininger, T.; Lorenz, R.D.; Totoki, E. Self-Sensing via Flux Injection with Rapid Servo Dynamics Including a Smooth Transition to Back-EMF Tracking Self-Sensing. *IEEE Trans. Ind. Appl.* **2020**, *56*, 2673–2684. [\[CrossRef\]](#)
3. Xiao, D.; Nalakath, S.; Filho, S.R.; Fang, G.; Dong, A.; Sun, Y.; Wiseman, J.; Emadi, A. Universal Full-Speed Sensorless Control Scheme for Interior Permanent Magnet Synchronous Motors. *IEEE Trans. Power Electron.* **2021**, *36*, 4723–4737. [\[CrossRef\]](#)
4. Wang, G.; Valla, M.; Solsona, J. Position Sensorless Permanent Magnet Synchronous Machine Drives—A Review. *IEEE Trans. Ind. Electron.* **2020**, *67*, 5830–5842. [\[CrossRef\]](#)
5. Kim, S.-I.; Im, J.-H.; Song, E.-Y.; Kim, R.-Y. A New Rotor Position Estimation Method of IPMSM Using All-Pass Filter on High-Frequency Rotating Voltage Signal Injection. *IEEE Trans. Ind. Electron.* **2016**, *63*, 6499–6509. [\[CrossRef\]](#)
6. Liu, J.M.; Zhu, Z.Q. Novel Sensorless Control Strategy with Injection of High-Frequency Pulsating Carrier Signal Into Stationary Reference Frame. *IEEE Trans. Ind. Appl.* **2014**, *50*, 2574–2583. [\[CrossRef\]](#)
7. Limsuwan, N.; Kato, T.; Yu, C.-Y.; Tamura, J.; Reigosa, D.D.; Akatsu, K.; Lorenz, R.D. Secondary Resistive Losses with High-Frequency Injection-Based Self-Sensing in IPM Machines. *IEEE Trans. Ind. Appl.* **2013**, *49*, 1499–1507. [\[CrossRef\]](#)
8. Gong, L.M.; Zhu, Z.Q. A Novel Method for Compensating Inverter Nonlinearity Effects in Carrier Signal Injection-Based Sensorless Control from Positive-Sequence Carrier Current Distortion. *IEEE Trans. Ind. Appl.* **2011**, *47*, 1283–1292. [\[CrossRef\]](#)
9. Raca, D.; Garcia, P.; Reigosa, D.D.; Briz, F.; Lorenz, R.D. Carrier-Signal Selection for Sensorless Control of PM Synchronous Machines at Zero and Very Low Speeds. *IEEE Trans. Ind. Appl.* **2010**, *46*, 167–178. [\[CrossRef\]](#)
10. Bianchi, N.; Bolognani, S.; Jang, J.-H.; Sul, S.-K. Advantages of Inset PM Machines for Zero-Speed Sensorless Position Detection. *IEEE Trans. Ind. Appl.* **2008**, *44*, 1190–1198. [\[CrossRef\]](#)
11. Zhang, X.; Li, H.; Yang, S.; Ma, M. Improved Initial Rotor Position Estimation for PMSM Drives Based on HF Pulsating Voltage Signal Injection. *IEEE Trans. Ind. Electron.* **2018**, *65*, 4702–4713. [\[CrossRef\]](#)
12. Xu, P.L.; Zhu, Z.Q. Carrier Signal Injection-Based Sensorless Control for Permanent-Magnet Synchronous Machine Drives Considering Machine Parameter Asymmetry. *IEEE Trans. Ind. Electron.* **2016**, *63*, 2813–2824. [\[CrossRef\]](#)
13. Ni, R.; Xu, D.; Blaabjerg, F.; Lu, K.; Wang, G.; Zhang, G. Square-Wave Voltage Injection Algorithm for PMSM Position Sensorless Control with High Robustness to Voltage Errors. *IEEE Trans. Power Electron.* **2017**, *32*, 5425–5437. [\[CrossRef\]](#)
14. Kim, D.; Kwon, Y.-C.; Sul, S.-K.; Kim, J.-H.; Yu, R.-S. Suppression of Injection Voltage Disturbance for High-Frequency Square-Wave Injection Sensorless Drive with Regulation of Induced High-Frequency Current Ripple. *IEEE Trans. Ind. Appl.* **2016**, *52*, 302–312. [\[CrossRef\]](#)
15. Hwang, C.-E.; Lee, Y.; Sul, S.-K. Analysis on Position Estimation Error in Position-Sensorless Operation of IPMSM Using Pulsating Square Wave Signal Injection. *IEEE Trans. Ind. Appl.* **2019**, *55*, 458–470. [\[CrossRef\]](#)
16. Lu, Q.; Wang, Y.; Mo, L.; Zhang, T. Pulsating High Frequency Voltage Injection Strategy for Sensorless Permanent Magnet Synchronous Motor Drives. *IEEE Trans. Appl. Supercond.* **2021**, *31*, 1–4. [\[CrossRef\]](#)
17. Yousefi-Talouki, A.; Pescetto, P.; Pellegrino, G.; Boldea, I. Combined Active Flux and High-Frequency Injection Methods for Sensorless Direct-Flux Vector Control of Synchronous Reluctance Machines. *IEEE Trans. Power Electron.* **2018**, *33*, 2447–2457. [\[CrossRef\]](#)
18. Haines, G.; Ertugrul, N. Wide Speed Range Sensorless Operation of Brushless Permanent-Magnet Motor Using Flux Linkage Increment. *IEEE Trans. Ind. Electron.* **2016**, *63*, 4052–4060. [\[CrossRef\]](#)
19. Liu, J.M.; Zhu, Z.Q. Rotor position error compensation based on third harmonic back-EMF in flux observer sensorless control. In Proceedings of the 2014 International Conference on Electrical Machines, Berlin, Germany, 2–5 September 2014; pp. 890–896.
20. Kivanc, O.C.; Ozturk, S.B. Sensorless PMSM Drive Based on Stator Feedforward Voltage Estimation Improved with MRAS Multiparameter Estimation. *IEEE/ASME Trans. Mechatron.* **2018**, *23*, 1326–1337. [\[CrossRef\]](#)
21. Chaoui, H.; Khayamy, M.; Aljarboua, A.A. Adaptive Interval Type-2 Fuzzy Logic Control for PMSM Drives with a Modified Reference Frame. *IEEE Trans. Ind. Electron.* **2017**, *64*, 3786–3797. [\[CrossRef\]](#)
22. Masmoudi, M.L.; Etien, E.; Moreau, S.; Sakout, A. Amplification of Single Mechanical Fault Signatures Using Full Adaptive PMSM Observer. *IEEE Trans. Ind. Electron.* **2017**, *64*, 615–623. [\[CrossRef\]](#)
23. Sreejith, R.; Singh, B. Sensorless Predictive Current Control of PMSM EV Drive Using DSOGI-FLL Based Sliding Mode Observer. *IEEE Trans. Ind. Electron.* **2021**, *68*, 5537–5547. [\[CrossRef\]](#)
24. Liang, D.; Li, J.; Qu, R. Sensorless Control of Permanent Magnet Synchronous Machine Based on Second-Order Sliding-Mode Observer with Online Resistance Estimation. *IEEE Trans. Ind. Appl.* **2017**, *53*, 3672–3682. [\[CrossRef\]](#)



25. Wang, G.; Yang, R.; Xu, D. DSP-Based Control of Sensorless IPMSM Drives for Wide-Speed-Range Operation. *IEEE Trans. Ind. Electron.* **2013**, *60*, 720–727. [\[CrossRef\]](#)
26. Zerdali, E.; Barut, M. The Comparisons of Optimized Extended Kalman Filters for Speed-Sensorless Control of Induction Motors. *IEEE Trans. Ind. Electron.* **2017**, *64*, 4340–4351. [\[CrossRef\]](#)
27. Yin, Z.; Gao, F.; Zhang, Y.; Du, C.; Li, G.; Sun, X. A review of nonlinear Kalman filter applying to sensorless control for AC motor drives. *CES Trans. Electr. Mach. Syst.* **2019**, *3*, 351–362. [\[CrossRef\]](#)
28. Shi, T.; Wang, Z.; Xia, C. Speed Measurement Error Suppression for PMSM Control System Using Self-Adaption Kalman Observer. *IEEE Trans. Ind. Electron.* **2015**, *62*, 2753–2763. [\[CrossRef\]](#)
29. Chen, Z.; Tomita, M.; Doki, S.; Okuma, S. New adaptive sliding observers for position- and velocity-sensorless controls of brushless DC motors. *IEEE Trans. Ind. Electron.* **2000**, *47*, 582–591. [\[CrossRef\]](#)
30. Qiao, Z.; Shi, T.; Wang, Y.; Yan, Y.; Xia, C.; He, X. New Sliding-Mode Observer for Position Sensorless Control of Permanent-Magnet Synchronous Motor. *IEEE Trans. Ind. Electron.* **2013**, *60*, 710–719. [\[CrossRef\]](#)
31. Liu, G.; Zhang, H.; Song, X. Position-Estimation Deviation-Suppression Technology of PMSM Combining Phase Self-Compensation SMO and Feed-Forward PLL. *IEEE J. Emerg. Sel. Top. Power Electron.* **2021**, *9*, 335–344. [\[CrossRef\]](#)
32. Sreejith, R.; Singh, B. Sensorless Predictive Control of SPMSM-Driven Light EV Drive Using Modified Speed Adaptive Super Twisting Sliding Mode Observer With MAF-PLL. *IEEE J. Emerg. Sel. Top. Ind. Electron.* **2021**, *2*, 42–52.
33. Liang, D.; Li, J.; Qu, R.; Kong, W. Adaptive Second-Order Sliding-Mode Observer for PMSM Sensorless Control Considering VSI Nonlinearity. *IEEE Trans. Power Electron.* **2018**, *33*, 8994–9004. [\[CrossRef\]](#)
34. An, Q.; Zhang, J.; An, Q.; Liu, X.; Shamekov, A.; Bi, K. Frequency-Adaptive Complex-Coefficient Filter-Based Enhanced Sliding Mode Observer for Sensorless Control of Permanent Magnet Synchronous Motor Drives. *IEEE Trans. Ind. Appl.* **2020**, *56*, 335–343. [\[CrossRef\]](#)
35. Vošmik, D.; Peroutka, Z. Sensorless control of permanent magnet synchronous motor employing extended Kalman filter in combination with HF injection method. In Proceedings of the 2011 14th European Conference on Power Electronics and Applications, Birmingham, UK, 30 August–1 September 2011; pp. 1–10.
36. Meng, Q.; Bao, G. Generalized Predictive Control of Permanent Magnet Synchronous Motor Based on Super Twisting Sliding Mode Observer. In Proceedings of the 2023 IEEE 6th International Electrical and Energy Conference (CIEEC), Hefei, China, 12–14 May 2023; pp. 2194–2199.
37. Lin, C.; Sun, S.; Yi, J.; Walker, P.; Zhang, N. Accelerated adaptive super twisting sliding mode observer-based drive shaft torque estimation for electric vehicle with automated manual transmission. *IET Intell. Transp. Syst.* **2019**, *13*, 160–162. [\[CrossRef\]](#)
38. Wang, D.; Liu, J.; Miao, S.; Yuan, T.; Li, Y.; Tian, W.; Liu, Z. Rotor Position estimation method for permanent magnet synchronous motor based on Super-Twisting Sliding Mode Observer. In Proceedings of the 2018 37th Chinese Control Conference (CCC), Wuhan, China, 25–27 July 2018; pp. 5634–5638.
39. Chen, Z.; Dawara, A.A.; Zhang, X.; Zhang, H.; Liu, C.; Luo, G. Adaptive Sliding Mode Observer-Based Sensorless Control for SPMSM Employing a Dual-PLL. *IEEE Trans. Transp. Electr.* **2022**, *8*, 1267–1277. [\[CrossRef\]](#)

**Disclaimer/Publisher’s Note:** The statements, opinions and data contained in all publications are solely those of the individual author(s) and contributor(s) and not of MDPI and/or the editor(s). MDPI and/or the editor(s) disclaim responsibility for any injury to people or property resulting from any ideas, methods, instructions or products referred to in the content.